Heat transport by parallel-roll convection in a rectangular container

By R. W. WALDEN, PAUL KOLODNER, A. PASSNER
AND C. M. SURKO

AT&T Bell Laboratories, Murray Hill, NJ 07974, USA

Heat-transport measurements are reported for thermal convection in a rectangular box of aspect ratio 10×5. Results are presented for Rayleigh numbers up to $35R_c$, Prandtl numbers between 2 and 20, and wavenumbers between 0.6 and $1.0k_c$, where R_c and k_c are the critical Rayleigh number and wavenumber for the onset of convection in a layer of infinite lateral extent. The measurements are in good agreement with a phenomenological model which combines the calculations of Nusselt number, as a function of Rayleigh number and roll wavenumber for two-dimensional convection in an infinite layer, with a nonlinear amplitude-equation model developed to account for sidewell attenuation. The appearance of bimodal convection increases the heat transport above that expected for simple parallel-roll convection.

1. Introduction

A long-standing problem of major interest in the study of thermal convection has been the measurement of heat transport as a function of the imposed temperature gradient. For a horizontal fluid layer heated from below, it has been recognized for many years (cf. Malkus 1954*a*, *b*) that a number of discrete transitions in heat transport occur as the temperature difference across the layer (in dimensionless terms, the Rayleigh number R) is increased. The first transition at the critical Rayleigh number R_c marks the onset of convection, usually with a two-dimensional pattern of parallel rolls. Above R_c the effective thermal conductivity of the fluid (in dimensionless terms, the Nusselt number N) increases steadily with R. However, as Malkus observed, there are several discontinuities in the rate of change of heat transport with increasing Rayleigh number, even in the regime of highly turbulent flow. Subsequent investigations (e.g. Willis & Deardorff 1967; Rossby 1969; Krishnamurti 1970*a*, *b*, 1973; Chu & Goldstein 1973; Threlfall 1975) verified Malkus' observations qualitatively but disclosed that the structure of the heat transport curve (e.g. the Rayleigh numbers at which transitions occur) depends significantly on factors such as the fluid properties (i.e. the Prandtl number σ) and the container geometry.

Some of these transitions in heat transport have now been associated with changes in the flow pattern. For example, for moderately large Prandtl numbers, the second transition (following onset of convection at R_c) occurs near $R = 12R_c$ and has now been identified with the onset of bimodal convection;† the next transition, near

---

† Bimodal convection, which is initiated by the cross-roll instability, involves the formation of parallel rolls in the horizontal boundary layer, superimposed at right angles to the original rolls.

$30R_c$, is evidently related to the onset of time dependence (Krishnamurti 1973). Additional transitions or 'kinks' in the slope of Nusselt versus Rayleigh number occur up to the largest Rayleigh numbers investigated experimentally ($\approx 10^7 R_c$), but the mean Nusselt number appears to approach a power-law dependence on Rayleigh number with an exponent which depends weakly on Prandtl number (Busse 1978).

For Rayleigh numbers $R \lesssim 100R_c$, it is now apparent that for laterally confined flows the parameters R and σ are not sufficient to specify the flow dynamics. However, within the entire domain for which the flow is substantially two-dimensional, we find that the heat transport and flow dynamics are consient with predictions that take into account roll wavenumber and container geometry as well as R and σ. We have studied convection in a rectangular box with dimensions 10×5 times the height. Pattern transitions are observed (Kolodner et al. 1986) that appear to correspond closely to the instabilities described by two-dimensional linear stability theory for a fluid layer of infinte horizontal extent (Busse 1978). The pattern transitions are always accompanied by a change in heat transport; and, provided the initial and final patterns are substantially two-dimensional, the heat transport is quantitatively consistent with the wavenumber-dependent predictions of the theory. Although no exact models are available to calculate the Nusselt number in a container of finite aspect ratio, in §4 we present an heuristic model which combines nonlinear calculations for an infinite layer with an amplitude equation model to account for finite-aspect-ratio effects.

2. Apparatus and procedure

2.1. Description of apparatus

The heat-transport and Rayleigh-number measurements reported here were done in conjunction with our studies of the stability of patterns described by Kolodner et al. (1986). The experiments were conducted in a rectangular box with a copper bottom plate and a sapphire top plate with interchangeable glass or acrylic walls. The interior dimensions of the containers are summarized in table 1. (Details of cell construction and materials are described by Kolodner et al. 1986.) The convection container is enclosed in a vacuum box, and a radiation shield surrounds the bottom plate of the container. The temperature of the top plate of the convection container was maintained constant to about ± 1 mK for extended periods of time. Prandtl numbers ($\sigma \equiv \nu/\kappa$, where ν is kinematic viscosity and κ is thermal diffusivity) ranging from 2.2 to 19 were achieved by varying the mean temperature of the working fluid (water or ethyl alcohol). Convection patterns were observed by directing a broad, collimated laser beam vertically on to the cell; the light reflected from the bottom plate and refracted by density variations in the fluid was projected on to a screen, and the image of the flow pattern was recorded on video tape.

In these experiments the top plate of the container was maintained at constant temperature while a steady heat flux was applied to the bottom plate. (Under conditions of constant heat flux the mean temperature difference ΔT across the fluid layer varies inversely with the effective thermal conductivity of the fluid.) The usual experimental procedure was to vary the heat flux in small steps, allow the system to settle, and measure ΔT. In the discussion that follows we express the temperature difference ΔT in terms of the dimensionless Rayleigh number $R = g\alpha\Delta T d^3/\kappa\nu$, where g is the acceleration due to gravity, α is the isobaric thermal expansion coefficient, and d is the height of the fluid layer; we express the heat flux Q in terms of the

	Aspect ratios			Wall
Cell	Γ_L	Γ_w	d (cm)	material
A	10.61	5.32	0.461	Acrylic
B	9.25	4.42	0.525	Glass

TABLE 1. Convection cells

dimensionless Nusselt number $N = Qd/\lambda S \Delta T$, where λ is the thermal conductivity of the fluid and S is the horizontal area of fluid layer.

2.2. *Nusselt-number measurements*

Accurate determination of the Nusselt and Rayleigh numbers required attention to both carefully measuring and minimizing sources and sinks of heat. Thermal shielding and evacuation of the apparatus minimized external convective and radiative heat flow. The major contributions to the bottom-plate heating were the 4-terminal wire-wound heater, the thermistors (one in a d.c. bridge, and usually one in an a.c. bridge circuit), and heating from the 15 mW He–Ne laser used for shadowgraphy.

Heating due to the a.c. bridge thermistor was negligible (≈ 4 µW). Heating due to the d.c. bridge thermistor was strongly temperature dependent (but accurately calibrated) and was typically ≈ 100 µW. The laser heating was also small (≈ 200 µW), with a slow variation over several months as the laser aged. By comparison, about 15–80 mW was required to reach R_c for these experiments. The 4-terminal measurements of heater power were accurate to an estimated $\pm 0.1\%$.

The bottom plate of the container was well radiation shielded from the upper (and colder) part of the apparatus. Heat transfer laterally through the sidewalls – due to radiation – was small at low Rayleigh numbers and assumed to be negligible. However, the container walls and the supporting frame provided a heat path parallel to the fluid. For example, heat transfer through the glass walls was about 80% of that through the water for $R < R_c$.

The thermal conductivity of the walls was determined for purposes of Nusselt-number determination using the measured thermal conductivity and temperature dependence of the wall material and estimating the effective wall area in contact with the upper and lower container boundaries. This effective area is less than the actual wall cross-section because of the O-rings and O-ring grooves at the contact surfaces. This (one constant) value of effective area was chosen to give N for $R < R_c$ at all operating temperatures. In fact, there was a slight increase in the effective thermal conductivity of the walls after the container was filled, probably owing to fluid filling the inner side of the O-ring grooves and effecting better heat transfer between the container wall and the sapphire plate.

The thermal conductivity of the copper bottom plate (about 660 times that of water) was sufficient to allow neglect of lateral gradients; and, indeed, thermistor measurements detected no lateral gradient except at very high Rayleigh number. However, the finite thermal conductivity of the sapphire top plate (about 50 times that of water) is not completely negligible. The maximum temperature difference across the sapphire can be estimated from the measured heat flux and the known thermal conductivity of the sapphire. However, because the sapphire plate is larger than the convection container and because of the finite thermal conductivity of the

Container	Prandtl number	Expt. R_c/R_{co}	Uncertainty in R_c/R_{co} $\pm(3\text{ mC}+2\%)$†	Uncertainty due to fluid parameters‖	Nusselt number
A	2.2	1.115	(0.038)‡	0.010	0.9752
	3.0	1.047	0.032	0.008	1.0070
	3.5	1.069	0.029	0.007	0.9683
	4.4	1.023	0.027	0.006	1.0106
	5.5	1.028	0.024	0.0015	1.0275
B	3.5	1.040	0.029	0.007	1.00¶
	11	1.056	0.059	0.03	
	15	0.998	0.043	0.03	
	19	0.988	0.034	0.03	

† Estimate of uncertainty in experimental determination of R_c/R_{co} (see text); tabulated values are equivalent to $(3\text{ mC}+2\%)$.

‡ During tests with Prandtl number 2.2 there was excessive drift in the computer-interfaced instrumentation (which subsequently required some major repairs); uncalibrated drift was at least 5% for some runs at this Prandtl number.

‖ Uncertainty in R/R_c due to uncertainty in the fluid parameters. The fluid parameters and estimated uncertainties are tabulated in Kolodner et al. (1986).

¶ Since the glass walls account for up to 80% of the heat transport when the cell is filled with ethanol, the temperature-dependent thermal conductivity of the walls was determined by requiring that $N = 1.00$ below R_c for each of the three highest Prandtl numbers. (Consistent values for wall thermal conductivity were obtained whether the cell was filled with water or with ethanol.)

TABLE 2. Critical Rayleigh and Nusselt numbers

container walls, the temperature of the sapphire surface which contacts the fluid in the convection container is non-uniform. The vertical temperature difference across the sapphire at R_c is approximately 1% of R_c. For the case of water with plastic walls, the temperature of the lower surface of the sapphire at the edges of the container is larger relative to the temperature of the sapphire at the centre of the container by about 0.5% of R_c at R_c. For the case of ethanol with glass walls, the temperature at the edges is depressed relative to the centre by about the same amount.

2.3. Sources of error

Uncertainties in the determination of Rayleigh and Nusselt numbers were normally dominated by fluctuations, drift and calibration uncertainties in the instrumentation for measuring the temperature of the bottom plate. Although temperature determinations to ± 1 mK were possible for individual measurements of the bottom-plate temperature, the normal procedure of computer-controlled runs of a least several days' duration between calibration times introduced uncertainties (both random and systematic) in determination of R and N. The uncertainties were typically expresssed as a combination of several components: (a) random noise in temperature measurement of ≈ 3 mK (including ≈ 1 mK fluctuation of the top-plate temperature); (b) uncalibrated nonlinearities and slow drift of the temperature-measurement instrumentation – about 1% of the *full-scale* temperature range for a given experimental run; and (c) uncertainty in the container depth and fluid properties used to compute Rayleigh number. In table 2 values of the critical Rayleigh number R_c are given together with estimated sources of error. (The procedure for calculation of Nusselt and Rayleigh numbers from the experimental measurements is described by Kolodner et al. 1986.)

3. Typical results

3.1. *Determination of critical Rayleigh number R_c*

For a laterally infinite fluid layer confined between fixed horizontal boundaries of high thermal conductivity, the critical Rayleigh number for onset of convection is $R_{co} = 1708$ (Chandrasekhar 1961). However, when the layer is confined by lateral boundaries, the onset of convection is generally suppressed until a higher Rayleigh number $R_c > R_{co}$. The experimental measurements of the critical Rayleigh number R_c are not of sufficient accuracy to definitively test existing models; however, it is appropriate to examine the differences between the values of R_c (as a function of aspect ratio) calculated from several numerical models.

A number of models for determination of R_c have been studied numerically. Although these studies individually are not matched to the parameter range or boundary conditions of our experiments, collectively they provide a reasonably coherent picture. Values of R_c, derived or extrapolated from several of these model calculations, are compared in table 3.

Values of R_c for fluid in a rectangular box with perfectly conducting sidewalls were computed by Davis (1967) and by Catton (1970) using 'finite-roll' trial functions with a Galerkin method which gives an upper limit for R_c. (The 'finite rolls' are defined as cells that have only two finite (non-zero) velocity components dependent on all three spatial variables.) Later Catton (1972*a*) extended his studies to boxes with insulating sidewalls. Catton's results are shown in figure 1, for which the calculated values of R_c are normalized by the expression $(\Gamma_x^a + \Gamma_y^b)$. Γ_x is the smaller of the two aspect ratios, and a and b are chosen to optimize the fit to the data.

Several numerical studies (Davies-Jones 1970, for a rectangular box with free horizontal boundaries and either insulating or conducting sidewalls; Charlson & Sani 1970, for a cylindrical box; and Catton 1972*b*, for rectangular boxes of very small aspect ratio) indicate that R_c is significantly smaller for insulating boundaries than for conducting boundaries for most aspect ratios.

In addition to exploring the effects of finite conductivity of the sidewalls, Davies-Jones demonstrated that the 'finite-roll' trial functions used in the Galerkin calculations are not exact solutions to the linearized convection problem, and that the true solutions always give lower values for R_c for any lateral boundary conditions. The Davies-Jones calculations, which assume free horizontal boundary conditions, were not extended to the rigid-boundary case, however.

Luijkx & Platten (1981) extended the work of Davis, Catton and Davies-Jones by the use of fully three-dimensional calculations for a rectangular box with insulating lateral boundaries and one infinite horizontal dimension. B. F. Edwards (1986, private communication), beginning with the same velocity expansion functions used by Catton (1972*a*) for a box with insulating sidewalls, has considered fully three-dimensional parallel rolls as well as crossed rolls. For boxes with nearly equal horizontal dimensions and small aspect ratio ($\Gamma < 12$) Edwards found that crossed rolls are clearly preferred because of their significantly smaller R_c.

Amplitude-equation calculations of R_c give an asymptotic formula for the critical Rayleigh number (Greenside & Coughran 1984; Wesfreid *et al.* 1978):

$$\epsilon_c \equiv \left(\frac{R_c}{R_{co}-1}\right) \approx \left[\frac{\pi\xi_0}{\Gamma_y}\right]^2 \quad \text{with } \Gamma_y \gtrsim \Gamma_x \gtrsim 4.$$

Here, $\xi_0^2 = 0.148$. Thus ϵ_c depends only on the *large* aspect ratio of the container,

| Container aspect ratios | Galerkin models | | | Amplitude-equation model‡ | Stork & Müller (1972) expt. |
| | Conducting walls† | Insulating walls | | | |
		Catton (1972a)	B. F. Edwards (1986, private communication)		
2×6	1.338	1.164	1.119	—	1.26±0.02
3×6	1.230	1.100	1.050	—	1.12
6×6	1.166	1.052	1.034	1.041	1.08
5.3×10.6	1.071±0.005	1.041±0.004	1.019±0.004	1.013±0.001	
4.4×9.3	1.10	1.055	1.026	1.017	

TABLE 3. Comparison of calculated critical Rayleigh numbers R_c/R_{c0}

† From the calculations of Catton (1970) and Davis (1967). The last two values (corresponding to the aspect ratios of our containers A and B) are estimated by extrapolation of their results.
‡ Amplitude-equation calculation (Greenside & Coughran 1984; Wesfreid et al. 1978).
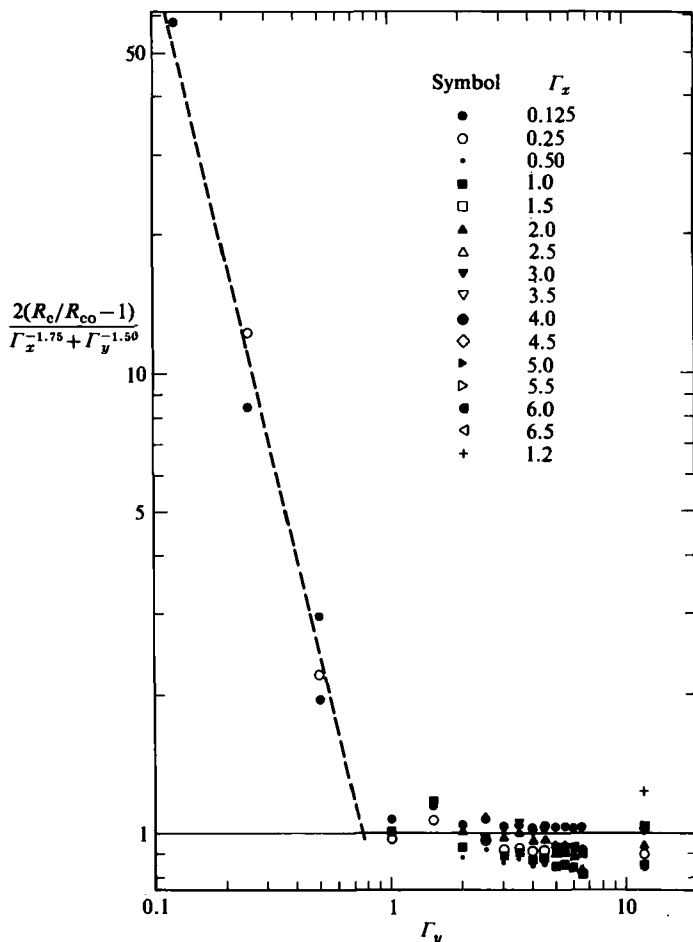
FIGURE 1. Calculations of R_c, the Rayleigh number for onset of convection, as a function of aspect ratio from Catton (1972 a). The calculated values of R_c are normalized by a simple function of the aspect ratios, Γ_x and Γ_y (with $\Gamma_x \leqslant \Gamma_y$), which facilitates comparison with other models. The dashed line is only a guide to the eye.

provided the small dimension is at least a few roll diameters. For the aspect ratios typical of our experiments, this model gives values of ϵ_c somewhat smaller than the Galerkin procedure (cf. table 3). The major qualitative difference between the Galerkin and amplitude-equation models is that, for the latter, ϵ_c depends primarily on the larger aspect ratio, while for the former, ϵ_c depends significantly on both aspect ratios.

Stork & Müller (1972) studied experimentally the onset of convection in small rectangular boxes with poorly conducting sidewalls. Their determinations of R_c generally lie between the predicted values of the models for insulating and conducting walls.

Our experimental determination of R_c (which should not depend on Prandtl number, but only on aspect ratio and properties of the container boundaries) seems to be consistent with the predictions of the models but is not of sufficient accuracy to distinguish among them (cf. tables 2 and 3). R_c is determined experimentally from observing the transition in Nusselt number as Rayleigh number is increased; in a few
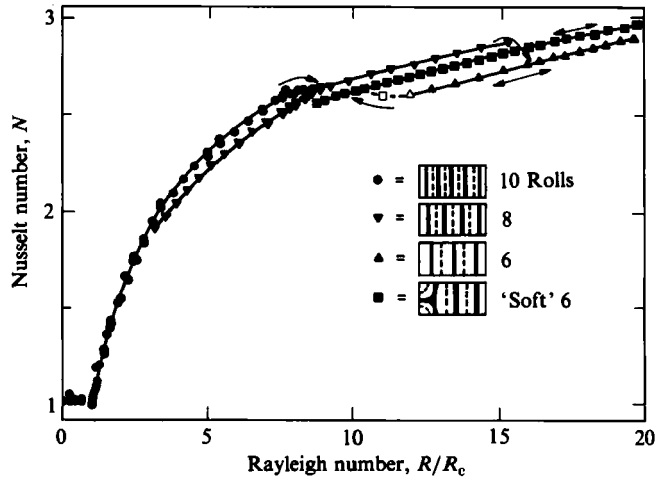
FIGURE 2. Nusselt number as a function of Rayleigh number measured for different convective patterns in Cell A for $\sigma = 5.5$. The roll patterns are illustrated schematically: the heavy solid lines represent up-flow boundaries and the dashed lines represent down-flow boundaries of adjacent rolls.

cases, these measurements were verified by visual observations using digital image processing. For $R \leqslant R_c$, the Nusselt number is exactly 1.0 by definition; therefore, departures from 1.00 in the experimentally determined values of N represent uncertainties in the fluid parameters or noise in the experimental measurements.

3.2. *Flow pattern transitions*

As the heat flux (and thus the Rayleigh number) is increased slowly, convection begins at the critical Rayleigh number R_c with a pattern of rolls parallel to the short side of the container. By means of transient heating, other patterns such as rolls parallel to the long side of the container can be initiated. In general, for Rayleigh numbers $R \gg R_c$ and $\sigma \lesssim 10$, transitions to parallel-roll patterns of smaller wavenumber (fewer rolls) are stimulated by instabilities such as the knot and skewed-varicose instabilities (see Kolodner *et al.* 1986). As the Rayleigh number is increased toward the critical value for such a transition, the convection pattern is progressively distorted. At the transition Rayleigh number the distortion begins to grow – very slowly at first – while the heat flux remains constant. Then, in the period of a few vertical diffusion times, a roll pair (or sometimes a single roll) is removed from the pattern. After the transition, the remaining rolls re-anneal to a simple parallel-roll pattern of approximately uniform wavenumber. After several such transitions other instabilities may be encountered with increasing Rayleigh number which result in complex three-dimensional patterns or sustained time-dependent behaviour or both. For Prandtl numbers $\sigma \gtrsim 10$ and $R \gg R_c$ the first instability encountered is usually the cross-roll instability, which results in 'bimodal' convection in which parallel rolls are formed in the horizontal boundary layer and superimposed at right angles to the original rolls. For still larger Rayleigh numbers, transitions to time dependence and more complex patterns occur.

The pattern distortions and subsequent transitions to smaller wavenumber which are observed for small Prandtl numbers are accompanied by a monotonically decreasing Nusselt number, while the appearance and growth of bimodal convection enhances the heat transport relative to that expected for two-dimensional parallel
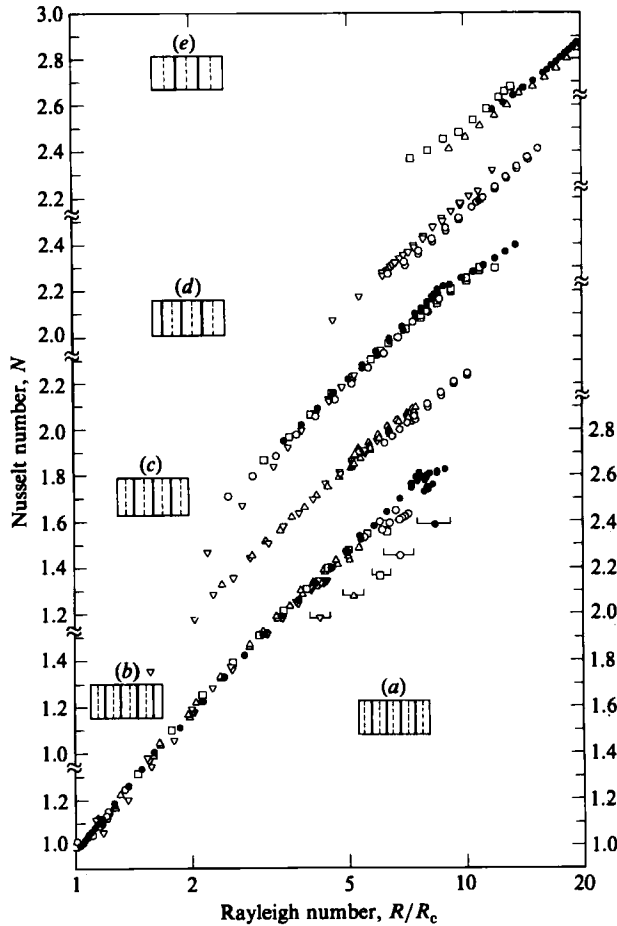
FIGURE 3. Experimental measurements of Nusselt number versus Rayleigh number for Cell A (see table 1). ●, $\sigma = 5.5$; ○, $\sigma = 4.4$; □, $\sigma = 3.5$; △, $\sigma = 3.0$; ▽, $\sigma = 2.2$. (a) Ten-roll pattern, (b) nine rolls, (c) eight rolls, (d) seven rolls, and (e) six rolls. The horizontal bars identify regions of pattern distortion due to the skewed-varicose instability. The vertical scales are the same for all the data with the zeros offset for each data set, as indicated on the left axis.

rolls. The transition to time dependence is often accompanied by pattern changes that obscure the explicit effects of time-dependent instabilities on the mean Nusselt number. A detailed description of these observations will be presented in §5.

3.3. *Heat transport*

An example of the pattern changes which occur with changing Rayleigh number and the consequent changes in Nusselt number is illustrated in figure 2 for $\sigma = 5.5$. Convection begins at R_c, with a pattern of ten rolls parallel to the short side of the container. This pattern is stable for $R \lesssim 7R_c$, and N increases monotonically with increasing R. When R is increased slowly above $7R_c$, the ten-roll pattern becomes progressively distorted; then a roll pair is ejected, leaving eight parallel rolls. Other hysteretic pattern transitions occur when R is changed further, as shown in figure 2. In general, Nusselt number decreases with decreasing roll wavenumber. This is consistent with the expectations of theory, to be described in §4.

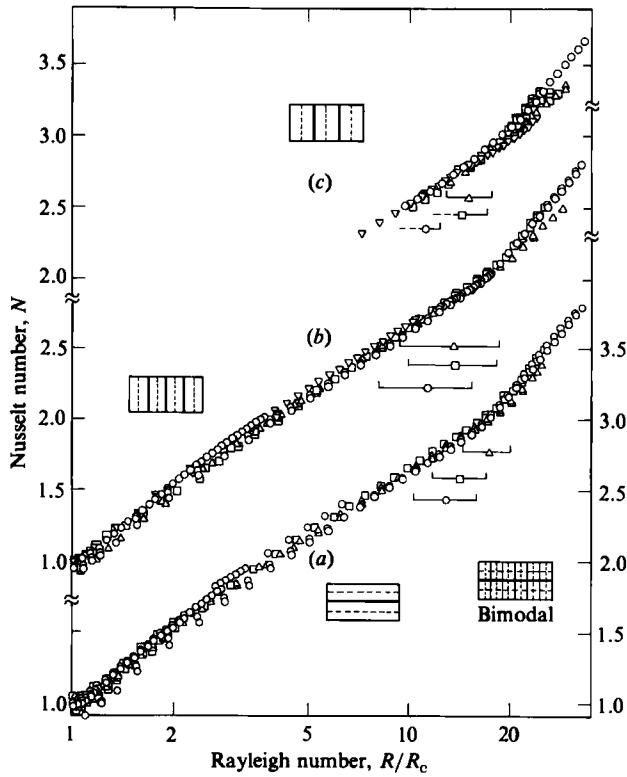The experimental measurements of Nusselt number are presented in figures 3 and

FIGURE 4. Experimental measurements of Nusselt number versus Rayleigh number for Cell B (see table 1). $\bigcirc$, $\sigma = 19$; $\square$, $\sigma = 15$; $\triangle$, $\sigma = 11$; $\triangledown$, $\sigma = 3.5$. (*a*) Flow pattern is four long rolls, (*b*) eight short rolls, (*c*) six short rolls. The horizontal bars identify the range of Rayleigh number for which bimodal convection grows in spatial extent.

4 for those cases in which the flow pattern is substantially two-dimensional so that roll wavenumber is well defined. Each section of figures 3 and 4 includes the data of all Prandtl numbers for a single mean wavenumber. The horizontal bars in figures 3(*a*) and 4(*a–c*) indicate the onset of substantial departures from two-dimensional flow. In figure 3(*a*), the bars indicate the range of substantial distortion of the flow pattern by the skewed-varicose instability just preceding the transition to a pattern of fewer rolls. In figure 4, the bars identify the gradual appearance of bimodal convection in response to the cross-roll instability. These transitions will be discussed further in §5.

4. A model for heat transport

It has long been recognized (cf. Segel 1969) that the presence of sidewalls (i.e. finite aspect ratio) suppresses convective heat transport and thus shifts the Nusselt number to a smaller value than that expected from the theory for infinite aspect ratio. A few of the recent experimental determinations of Nusselt number verify this prediction (cf. table 4); however, previous measurements of Nusselt number have usually been made in the absence of information about wavenumber, which is an essential parameter for comparison with theory.

There are two standard approaches to computation of the hydrodynamic variables (velocity, temperature, and heat transport) in Rayleigh–Bénard convection, neither

Author(s)	Container aspect ratio	Prandtl number	Range of R studied	$dN/dR\|_{R_c}^+$	At wavenumber
Ahlers et al. (1981) and Behringer & Ahlers (1982)	Circular $R/d = 4.72$	0.78	$R_c \lesssim R \lesssim 1.08 R_c$	$0.840 + 1.28\epsilon$	? (perhaps $2.972 = 9$ rolls)
Motsay, Anderson & Behringer (1988)	Rectangular 13.4×5.95	0.70	$R_c \lesssim R \lesssim 12 R_c$	0.56	2.81 ?
	Rectangular 18.2×8.12	0.52	$R_c \lesssim R \lesssim 12 R_c$	0.70	3.11 ?
Schluter et al. (1965)	Theory, $\Gamma = \infty$ parallel rolls	0.78 0.70 0.52		1.414 1.409 1.387	3.117

TABLE 4. Influence of finite aspect ratio on Nusselt number†

† Many other measurements of heat transport have been reported (cf. Rossby 1969), but these results generally do not illustrate the effects of finite aspect ratio.

of which is entirely satisfactory for comparison with our experimental data. The first approach involves computations using the full, nonlinear fluid equations assuming a two-dimensional convective flow. It has the advantage that good results are possible for all values of the parameter space (Rayleigh number, wavenumber, and Prandtl number) for which two-dimensional convection is stable. However, these two-dimensional models do not account for the effects of finite aspect ratio. The other approach is the amplitude-equation model, which is an expansion to lowest order in $\epsilon = (R/R_c - 1)$ of the hydrodynamic equations. This model is accurate only for rather small ϵ, but it can account well for the flow attenuation due to the imposition of finite lateral boundaries.

We have explored an intuitive model which takes advantage of the strengths of both traditional approaches – combining the Rayleigh-number, Prandtl-number, and wavenumber dependence of the two-dimensional models with the aspect-ratio dependence of the amplitude-equation model. As Segel (1969) observed from his amplitude-equation studies of convection in a laterally bounded layer, the mean amplitude of convection in the interior of the layer is nearly the same as for an unbounded layer, while the flow attenuation due to the lateral walls is confined primarily to a well-defined boundary layer at the walls. According to Segel's calculations (which assume free horizontal boundaries), when the Rayleigh number is 5 or 10 % above R_{co}, the effects of the lateral walls should be confined to a boundary layer whose thickness is of the order of a wavelength (that is, the width of a roll pair). However, more generally, the width and profile of the boundary layer depend on the orientation of the rolls with respect to the sidewalls (Zaleski, Pomeau & Pumir 1984). Thus our heuristic model for Nusselt number contains the effects of finite aspect ratio essentially as an attenuation of the flow amplitude in a boundary layer adjacent to each sidewall, with attenuation computed separately for walls parallel to and perpendicular to the convective rolls. Specifically, the calculations for an infinte layer are multiplied by aspect-ratio-dependent factors which account for the sidewall attenuation. While the amplitude-equation model should not be expected to represent accurately the aspect-ratio dependence of the Nusselt number for $\epsilon \gg 1$, it does remarkably well when the model is compared with the experimental data (§5). We begin by reviewing each of the components of the combined model, and conclude in §4.3 with further discussion of the utility and limitations of this model.

4.1. *The nonlinear two-dimensional model*

There have been a number of nonlinear calculations of heat transport across a laterally infinite fluid layer assuming two-dimensional parallel-roll convection (Busse 1967; Plows 1968; Denny & Clever 1974; Clever & Busse 1974). These authors have employed several different computational techniques (e.g. Galerkin and finite-difference methods), and the results obtained by the various techniques are generally in good agreement with each other. In order to compare our experimental results with these calculations, the calculated Nusselt number $N_\infty(\epsilon, k, \sigma)$ has been parameterized as a function of reduced Rayleigh number ϵ, wavenumber k, and Prandtl number σ.

For two-dimensional convection in a laterally infinite box the Nusselt number $N_\infty(\epsilon, k, \sigma)$ is parameterized primarily from the calculations of Busse (1967) and Clever & Busse (1974),† since together they provide a consistent set of data over a

---

† Willis, Deardorff & Somerville (1972) presented a simple parameterization of the Nusselt number as a function of R, k, and σ; however, the parameter range for its validity and the degree of accuracy were not sufficient for satisfactory comparison with our experimental data.
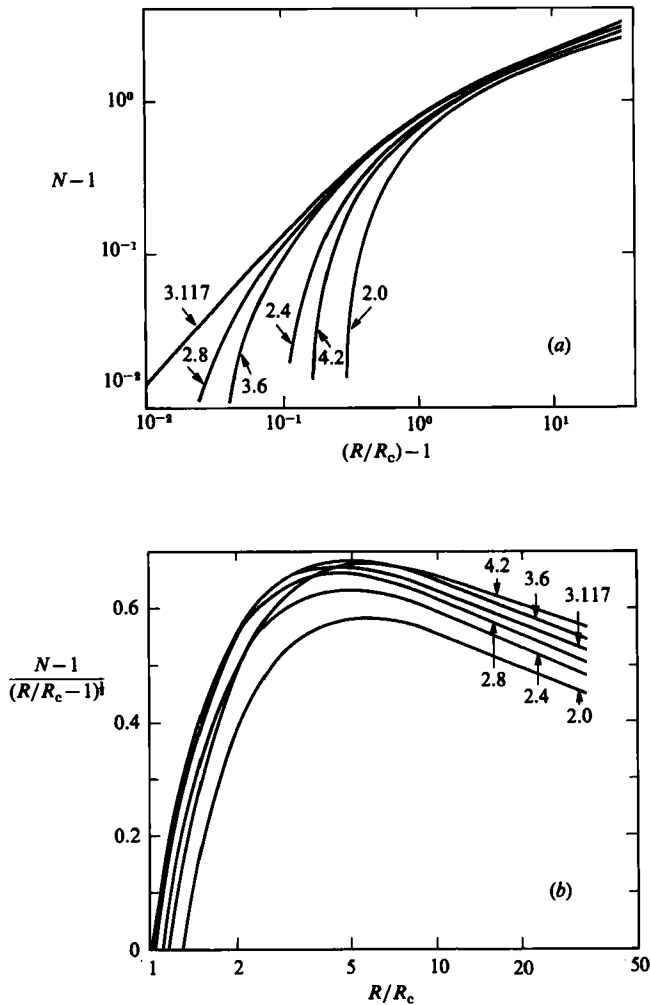
FIGURE 5. Nusselt number as a function of Rayleigh number for various values of the wavenumber with $\sigma = 7$ from the model of §4.1. (a) small R/R_c (plotted on a log–log scale); (b) large R/R_c (linear scale). The quantities plotted on each axis are chosen to illustrate clearly the Rayleigh-number and wavenumber dependence of the Nusselt number.

wide parameter range. Both works use a Galerkin procedure, starting from the Oberbeck–Boussinesq approximation to the Navier–Stokes equations. The calculations of Busse (1967) are for infinite Prandtl number, while Clever & Busse (1974) present results for $\sigma = 7$ and for several values of $\sigma < 1$. The model also incorporates the neutral stability curve, $R_c(k)$ (cf. Chandrasekhar 1961). These data are combined into a 35-parameter model using nonlinear interpolation algorithms such as nonlinear least squares. The resulting fit, which is illustrated in figures 5 and 6, has smooth derivatives while matching the input data to better than 1% (0.1% is typical). In fact, our fit also matches the data of Plows (1968) and Lipps & Somerville (1971) to better than 1% and is consistent with the predicted slope dN/dR near R_c (Schluter, Lortz & Busse 1965 and Clever & Busse 1974).

Our fit is optimized for $\sigma = 7$ since the agreement between different sources is best near this Prandtl number (cf. figure 7). Although for $\sigma \gg 1$ our model closely
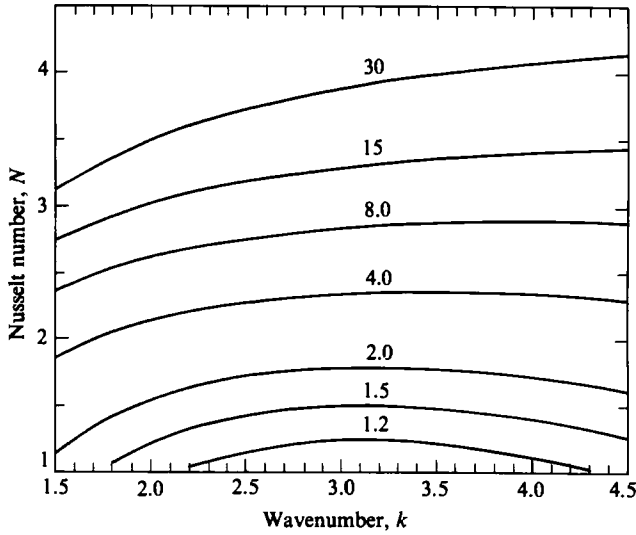
FIGURE 6. Nusselt number as a function of wavenumber for various values of the Rayleigh number with $\sigma = 7$ from the model of §4.1.
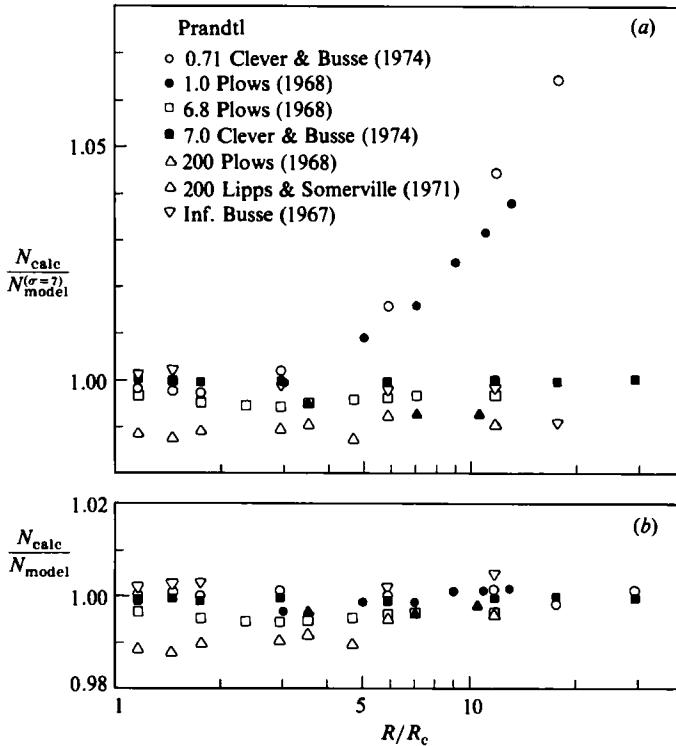

FIGURE 7. Comparison of various calculations of Nusselt number with our 'model'. Calculations are for infinite aspect ratio and wavenumber $k_c = 3.117$. (a) N_{calc} compared with model at fixed Prandtl number ($\sigma = 7$); (b) N_{calc} compared with model (Prandtl number same as the experimental σ).
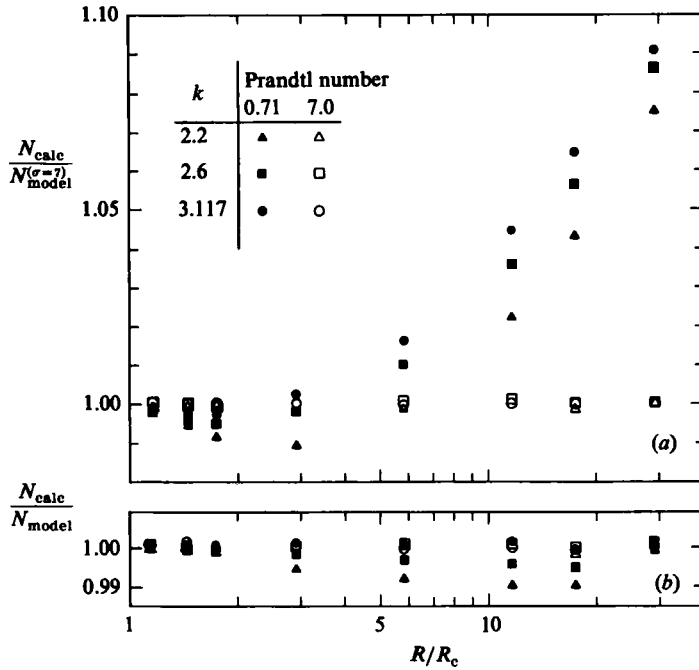
FIGURE 8. Comparison of Nusselt number calculations of Clever & Busse (1974) with our model for several wavenumbers and small Prandtl numbers. (a) Prandtl number of the model fixed at $\sigma = 7$; (b) Prandtl number of model matched to calculations.

approximates the calculations of Busse (1967), the Prandtl-number dependence of the Nusselt number is very weak, and even the sign of change in N with increasing σ is uncertain from comparison of the several calculations. For $\sigma < 7$, Prandtl-number dependence is more significant, but calculated data are sparse, especially for wavenumbers away from $k_c = 3.117$ (cf. figure 8). Nevertheless, the model should be accurate within 1 % for all $\sigma \gtrsim 1$.

4.2. *The amplitude equation and the effect of sidewalls*

The amplitude equation was first derived by Newell & Whitehead (1969) and Segel (1969) for the case of free horizontal boundaries and later extended by Wesfreid *et al.* (1978) and Cross (1980) to the case of rigid boundaries. The amplitude equation, which is derived from the full Boussinesq approximation to the hydrodynamic equations, describes the slow temporal and spatial variations of velocity and temperature near the onset of convection in terms of a real order parameter $\Psi(r, t)$. Conventionally, Ψ is normalized so that the convective heat flux is given by

$$\frac{S(N-1)R}{R_c} = \int d^2 r |\Psi|^2,$$

where S is the area of the container, N is the Nusselt number, and R_c is the critical Rayleigh number for onset of convection. It is convenient to write the amplitude equation in the form (Ahlers *et al.* 1981)

$$\frac{\partial \Psi}{\partial t} = \frac{1}{\tau_0}\left[\epsilon - \frac{\xi_0^2}{4q_0^2}(\nabla^2 + q_0^2)^2 - g\Psi^2\right]\Psi, \tag{1}$$

8

where τ_0 and g are functions of Prandtl number, $\epsilon = R/R_c$, and ξ_0^2 is the curvature of the neutral stability curve at the critical wavevector q_0.

For a system of convective rolls with axes parallel to the y-direction, the solution to (1) can be written

$$\Psi(r, t) = \sqrt{2} \, \mathrm{Re}\,[A(r, t)\,\mathrm{e}^{iq_0 x}], \qquad (2)$$

where $A(r, t)$ is a slowly varying complex function. For steady convection $\partial A/\partial t = 0$, and the amplitude equation (1) becomes (Newell & Whitehead 1969; Ahlers *et al.* 1981)

$$\left[\epsilon + \xi_0^2 \left(\frac{\partial}{\partial x} - \frac{i}{2q_0}\frac{\partial^2}{\partial y^2}\right)^2 - g|A|^2\right] A = 0. \qquad (3)$$

If lateral boundaries are now imposed on the flow, the mechanical boundary condition at the sidewalls is expressed by

$$\Psi = \hat{n}\cdot\nabla\Psi = 0, \qquad (4)$$

where $\hat{n}$ is the unit vector perpendicular to the lateral boundary (Zaleski *et al.* 1984).

The lateral boundary conditions have been derived only for the case of free upper and lower boundaries with 'ideal' sidewalls which are perfectly insulating or perfectly conducting (Brown & Stewartson 1977). It has been shown that the boundary conditions for sidewalls parallel to the rolls are not affected by the thermal conductivity of the walls to lowest order in ϵ (Cross *et al.* 1980), provided there is no net heat transfer through the walls (Ahlers *et al.* 1981). Since (4) is sufficient at least to lead to a well-defined solution to the amplitude equation, we shall not tackle the more difficult problem of defining the appropriate thermal boundary conditions (studied for special cases by Cross *et al.* 1983 and Daniels 1977).

We now derive expressions for the attenuation of Nusselt number due to the presence of sidewalls by calculating the boundary-layer profile for rolls parallel to sidewalls and for rolls perpendicular to sidewalls.

4.2.1. *Rolls parallel to sidewalls*

Consider first a system of convective rolls parallel to the y-axis (figure 9a), infinite in length, but confined between sidewalls at $x = 0$ and $x = L$. At least for large ϵ or large L (and following the experiments of Wesfreid *et al.* 1978) we expect the solution to give rolls of nearly uniform amplitude away from the boundaries, and that the amplitude will be substantially attenuated within the boundary layer near each sidewall. Equation (3) now reduces to

$$\left[\epsilon + \xi_0^2\left(\frac{\partial^2}{\partial x^2}\right) - g|A_1|^2\right] A_1 = 0. \qquad (5)$$

The full spatial dependence of Ψ is given by $\Psi = A_1(x)\sin(q_0 x + \phi)$, and the boundary conditions (4) require that $\phi = 0$ and $A_1 = 0$ at $x = 0, L$. The solution to (5), which is discussed in Appendix A, gives the Nusselt number N as the product of two parts:

$$\frac{(N-1)R}{R_c} = |\Psi|^2 = f(\epsilon)\,\alpha_1(\epsilon, L),$$

where $f(\epsilon)$ is the asymptotic solution for $L \rightarrow \infty$ (infinite aspect ratio) and $\alpha_1(\epsilon, L)$ represents the attenuation due to the presence of the lateral boundaries.
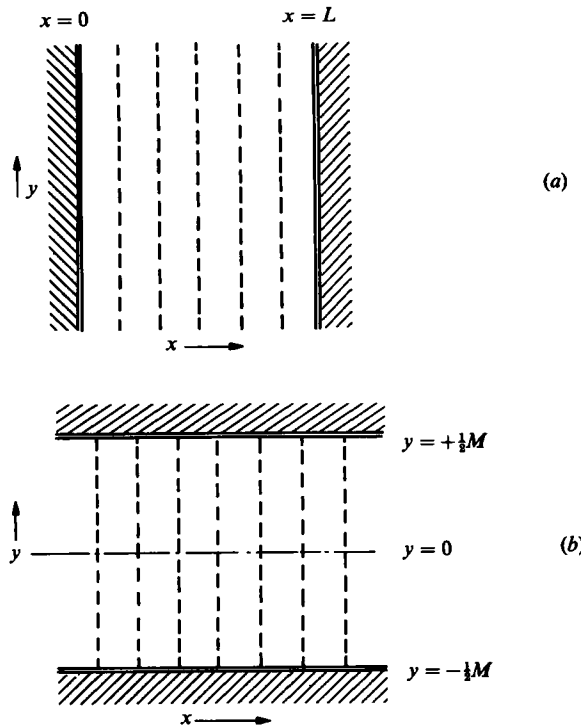
FIGURE 9. (*a*) Infinite rolls parallel to rigid sidewalls; (*b*) rolls perpendicular to rigid sidewalls.

4.2.2. *Rolls perpendicular to sidewalls*

Now consider an infinite system of convective rolls parallel to the *y*-axis and confined between sidewalls at $y = \pm\frac{1}{2}M$ (figure 9*b*). Again, for large ϵ or large M we expect the rolls to be of uniform amplitude away from the boundaries (i.e. near $y = 0$), and that the amplitude will be substantially attenuated within the boundary layer at the roll ends. For this case (3) reduces to

$$\left[\epsilon - \frac{\xi_0^2}{q_0^2}\left(\frac{\partial^4}{\partial y^4}\right) - g|A_2|^2\right]A_2 = 0, \tag{6}$$

with $\Psi = A_2(y) \sin(q_0 x + \phi)$ and ϕ arbitrary. From (4) the boundary conditions are $A_2 = \partial A_2/\partial y = 0$ at $y = \pm\frac{1}{2}M$. The solution to (6), which is discussed in Appendix B, gives a Nusselt number in the form

$$\frac{(N-1)R}{R_c} = |\Psi|^2 = f(\epsilon)\,\alpha_2(\epsilon, M),$$

where $f(\epsilon)$ is the asymptotic solution defined above and $\alpha_2(\epsilon, M)$ represents the attenuation due to the presence of the end boundaries.

4.3. *The combined model*

We now combine the models discussed in §§4.1 and 4.2 so that

$$N = [N_\infty(\epsilon, k, \sigma) - 1]\,\alpha_1(\epsilon, L)\,\alpha_2(\epsilon, M) + 1.$$

It is expected that the picture of flow attenuation in a boundary layer adjacent to each sidewall is qualitatively correct for Rayleigh number and aspect ratio moderately large, and the experimental data in §5 are in good agreement with this picture. However, several limitations of the model deserve discussion.

For small aspect ratio or small ϵ (i.e. for $\epsilon^{\frac{1}{2}} \Gamma_x \lesssim \epsilon^{\frac{1}{2}} \Gamma_y \lesssim 1$) the problem is clearly not two-dimensional, and separation of (x, y) variables as we did to obtain the coefficients α_1, α_2 is not valid. Furthermore, for small ϵ and Γ the rolls are not strictly two-dimensional; as pointed out in §3, departures from the 'finite-roll' approximation decrease R_c and, of course, affect heat transport as well.

For ϵ and Γ large, the amplitude envelope requires higher-order terms in k and ϵ to properly account for sidewall attenuation. On the other hand, the sidewall boundary layers in this case represent only a small fraction of the fluid layer, so that a moderately large adjustment to the boundary-layer amplitude may imply only a small change in the total heat transport.

5. Comparison of data with the model

The experimental measurements of Nusselt number were presented in figures 3 and 4 for those cases in which the flow pattern is substantially two-dimensional so that the roll wavenumber is well defined. In figures 10 and 11 the experimental data have been normalized by a calculated Nusselt number derived from the phenomenological model presented in the preceding section. In order to facilitate the best comparison possible, the experimental Nusselt and Rayleigh numbers were adjusted to compensate for the offset errors indicated in table 2; that is, for each Prandtl number, all the data were compensated by the amount required so that $\bar{N} = 1$ for $R < R_c$, where $\bar{N}$ is the mean experimental Nusselt number. Similarly the experimentally determined R_c was shifted to match the critical Rayleigh number of the model. As table 2 implies, these adjustments are collectively random in sign and magnitude, so that the primary effect of compensation is to reduce the large scatter in the data at small Rayleigh numbers.

Each section of figures 10 and 11 includes the data of all Prandtl numbers for a single mean wavenumber. Within the scatter of the data it is clear that the model of §4 provides a useful representation of the Nusselt number as a function of the five variables: R, k, σ, Γ_x, and Γ_y.

Figures 10(a) and 11(a–c) illustrate the effect of significant departures from two-dimensional flow. In figure 10(a), the skewed-varicose instability is responsible for the transition at large Rayleigh number to a pattern of fewer rolls. This transition is preceded (in Rayleigh number) by substantial distortion of the flow from a pattern of parallel rolls which results in a decrease in the Nusselt number. The range of R of the pattern distortion is identified for each Prandtl number by the horizontal bars; the transition Rayleigh number increases with increasing Prandtl number. Figures 10(c–f) show data from patterns of successively longer wavelength. In figure 10, the sidewall attenuation factor $(\alpha_1 \alpha_2)$ used in normalizing the data is, for example, 0.654 at $1.5R_c$, 0.811 at $5R_c$, and 0.878 at $20R_c$.

As shown in figure 11, the appearance of bimodal convection in response to the cross-roll instability at large Rayleigh numbers is reflected in a corresponding increase in Nusselt number. As Rayleigh number is increased, bimodal convection first begins near the corners of the fluid layer and grows in intensity and spatial extent with increasing Rayleigh number until it covers the entire fluid layer. The horizontal bars in figure 11 indicate the range in Rayleigh number for which bimodal
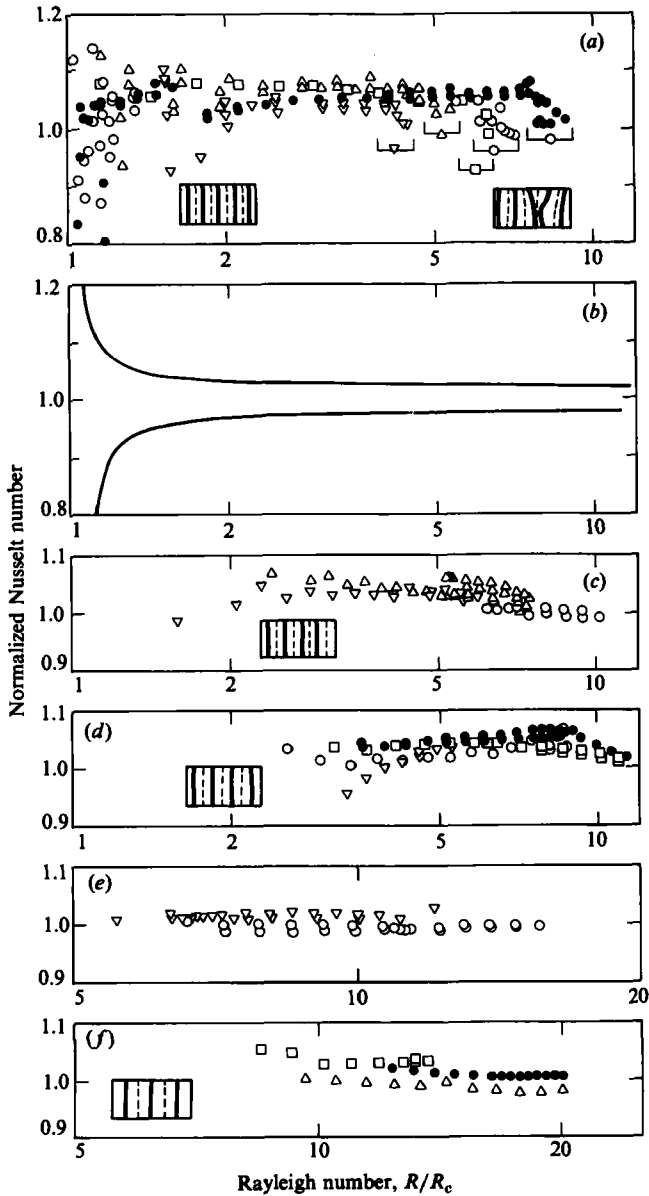
FIGURE 10. Experimental measurements of Nusselt number normalized by the model calculations $N(R, \sigma, k, \Gamma_1, \Gamma_2)$ versus Rayleigh number. Γ_1 and Γ_2 are fixed (see table 1 : Cell A); R, σ, and k are chosen to match the experimental conditions. ●, $\sigma = 5.5$; ○, $\sigma = 4.4$; □, $\sigma = 3.5$; △, $\sigma = 3.0$; ▽, $\sigma = 2.2$. (*a*) Ten-roll pattern, (*b*) estimated uncertainty in experimental results, (*c*) nine-roll pattern, (*d*) eight rolls, (*e*) seven rolls, and (*f*) six rolls. The horizontal bars identify pattern distortion due to the skewed-varicose instability.

convection grows in its spatial extent, starting at the corners, until it fills the container. The Rayleigh number for which bimodal convection appears is Prandtl-number-dependent, but in each case the measurable increase in Nusselt number begins with Rayleigh numbers just above those for which full bimodal convection occurs. The Rayleigh numbers at which these transitions occur is somewhat
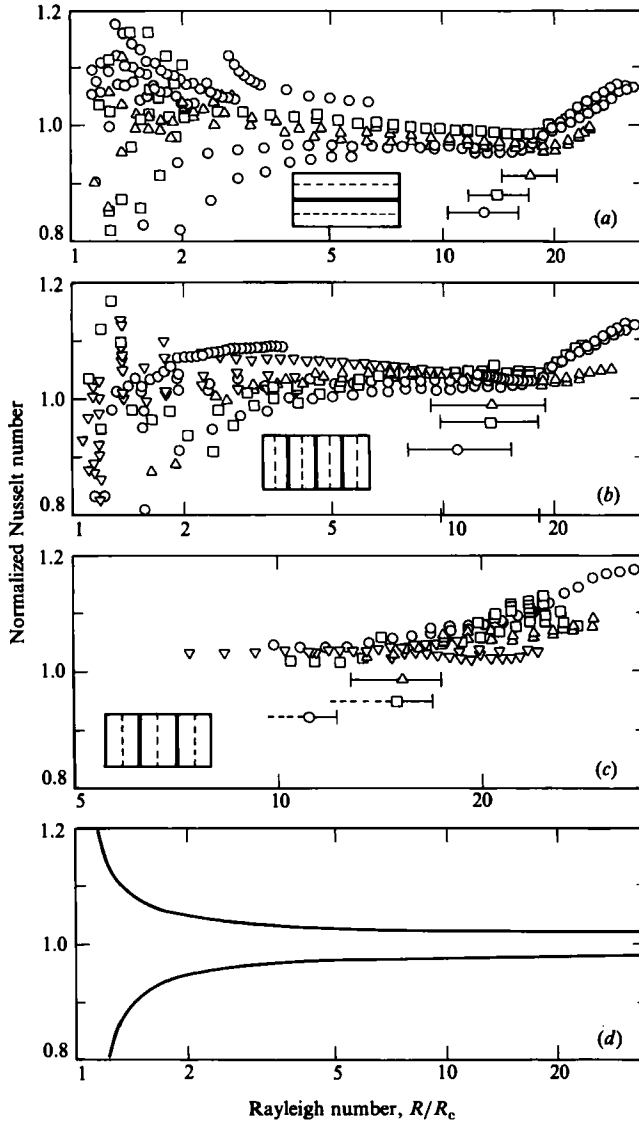
FIGURE 11. Experimental measurements of Nusselt number normalized by the model calculations $N(R, \sigma, k, \Gamma_1, \Gamma_2)$ versus Rayleigh number. Γ_1 and Γ_2 are fixed (see table 1: Cell B); R, σ, and k are chosen to match the experimental conditions, $\bigcirc$, $\sigma = 19$; $\square$, $\sigma = 15$; $\triangle$, $\sigma = 11$; and $\bigtriangledown$, $\sigma = 3.5$. (a) Flow pattern is four long rolls, (b) eight short rolls, (c) six short rolls; (d) typical uncertainty in experimental results. The horizontal bars identify the range of Rayleigh number for which bimodal convection grows in spatial extent.

subjective, since the transitions are continuous and gradual with changing Rayleigh number. In the case of figure 11(c), convection at this wavenumber ($k = 2.04$) is unstable to the cross-roll instability for all Rayleigh numbers when $\sigma \gtrsim 15$, so that the pattern is not really two-dimensional for any Rayleigh number. However, the appearance of full bimodal convection is still well defined in Rayleigh number and corresponds to the onset of an enhancement to Nusselt number.

Observations of Nusselt number at the onset of time-dependence are shown in figure 12 for two Prandtl numbers. In each case the initial flow pattern is six parallel
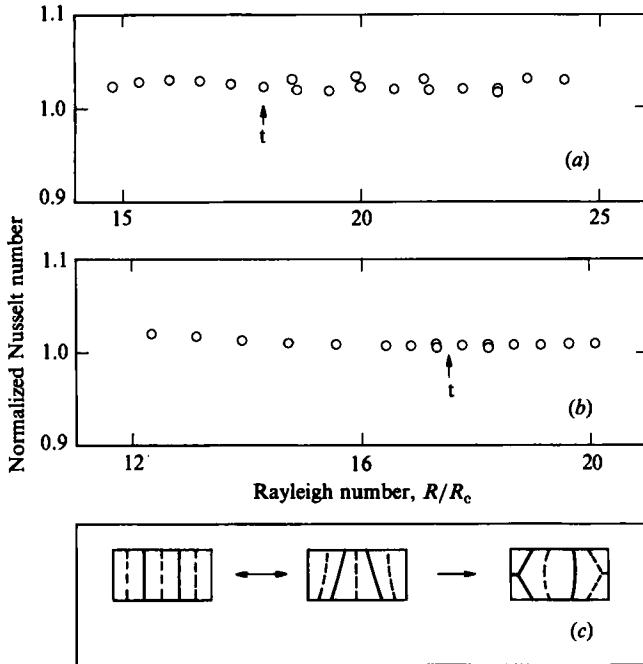
FIGURE 12. Experimental measurements of Nusselt number normalized by the model calculations $N(R, \sigma, k, \Gamma_1, \Gamma_2)$ versus Rayleigh number, showing the onset of time dependence (marked t). (*a*) $\sigma = 3.5$; (*b*) $\sigma = 5.5$; (*c*) schematic representation of flow pattern evolution with increasing Rayleigh number (see text).

rolls. The pattern becomes slightly distorted with increasing Rayleigh number as shown in the centre illustration of figure 12(*c*), and time dependence begins as a standing-wave oscillation localized near one corner of the container (Walden *et al.* 1984). With increasing Rayleigh number one or more additional modes appear and the oscillations grow in amplitude until the parallel-roll pattern breaks up into a more complex pattern with chaotic time-dependent behaviour. The shape of the pattern distortion varies somewhat from one trial to another, and consequently so does the sequence of transitions with increasing R leading to the pattern break-up. For example, we have observed as few as two and as many as five independent oscillatory modes prior to the appearance of chaotic time-dependent behaviour.

The observations of Nusselt number show no measurable change in the time-averaged heat transport (relative to the two-dimensional model), even when the oscillation amplitude represents several per cent in Nusselt number.

For Prandtl numbers $\sigma \gtrsim 10$ the onset of bimodal convection generally occurs at smaller Rayleigh numbers than the onset of time dependence. The model of Frick, Busse & Clever (1983), using a three-dimensional Galerkin calculation for a fluid layer of infinite horizontal extent, shows that bimodal convection enhances heat transport by as much as $2\frac{1}{2}\%$ at $15R_c$ and by as much as 12% at $29R_c$. The enhancement is a function of R, k, and σ as well as a strong function of the secondary roll (cross-roll) wavenumber $\tilde{k}$. A good quantitative comparison with our experimental results is not possible for two reasons. (i) The secondary roll wavenumber $\tilde{k}$ is not always well defined experimentally (see Kolodner *et al.* 1986), and (ii) the calculations of Frick *et al.* for a limited range of parameters cannot be
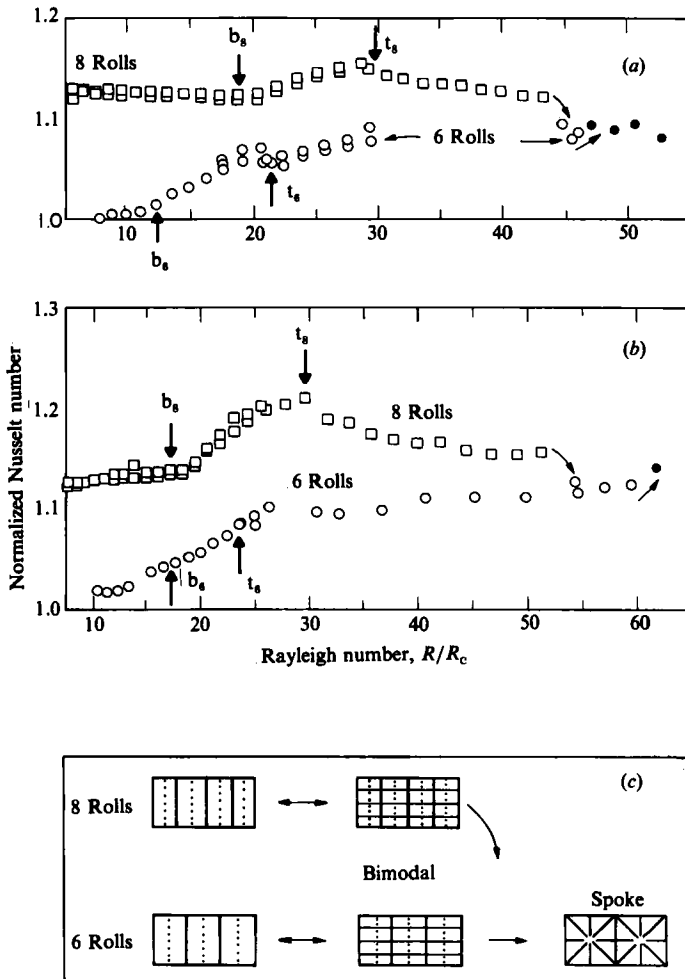
FIGURE 13. Experimental measurements of Nusselt number normalized by the model calculations $N(R, \sigma, k, \Gamma_1, \Gamma_2)$ versus Rayleigh number, showing the effects of bimodal and time-dependent convection. Values of N are computed assuming a pattern of six parallel rolls. b and t indicate respectively the onset of bimodal convection and the onset of time dependence; the subscripts indicate the number of rolls in the flow pattern. (a) $\sigma = 11$; (b) $\sigma = 14$; (c) schematic representation of the flow pattern evolution with changing Rayleigh number. ○, six rolls; □, eight rolls; ●, spoke pattern.

reliably extrapolated to the range of our experimental data. In particular, the experimental values of k are all smaller than the critical wavenumber k_c, while the calculations are for $k \gtrsim k_c$.

In spite of these limitations, the experimental data (figure 13) show that bimodal convection produces enhancement of the heat transport, which is quantitatively consistent with the calculations of Frick et al. The arrows 'b_6' and 'b_8' in figure 13 identify the appearance of bimodal convection throughout the convection cell. As indicated earlier (in figure 11 b, c) however, cross-rolls appear at the corners of the cell at smaller Rayleigh numbers and expand to permeate the cell with increasing Rayleigh number. Heat transport for the six-roll patterns seems to show some evidence of the effects of bimodal convection just after the appearance of corner rolls,
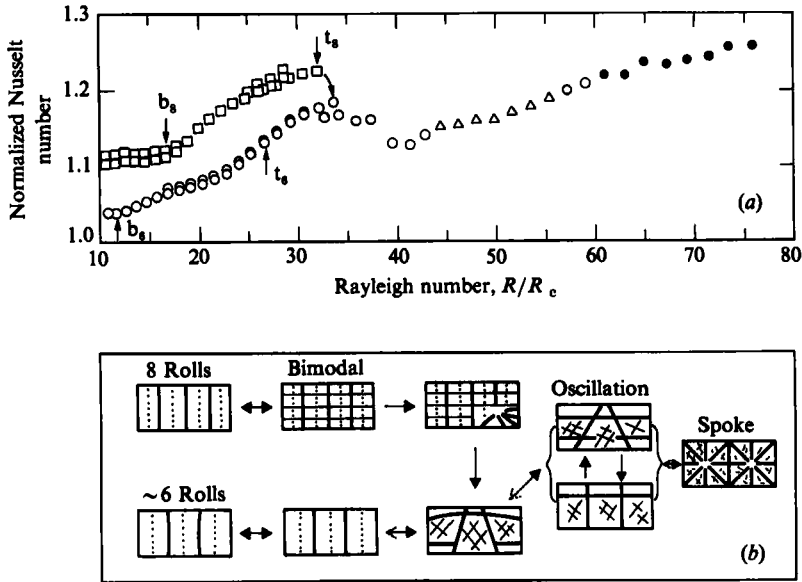
FIGURE 14. (a) Experimental measurements of Nusselt number normalized by the model calculations $N(R, \sigma, k, \Gamma_1, \Gamma_2)$ versus Rayleigh number showing the onset of time dependence for $\sigma = 19$. Values of N are computed assuming a pattern of six parallel rolls. b and t indicate respectively the onset of bimodal convection and the onset of time dependence. (b) Schematic representation of flow pattern evolution with changing Rayleigh number. $\bigcirc$, six rolls; $\square$, eight rolls; $\triangle$, pattern oscillation; $\bullet$, spoke pattern.

but in all cases there is a sharp increase in Nusselt number after the appearance of full bimodal convection.

Another feature common to these figures is a transition in dN/dR (the rate of change of heat transport with changing Rayleigh number) near the onset of time dependence. Although the onset of time dependence may be associated with subtle changes in the flow pattern which also affect heat transport, we have no intuitive explanation of this observation. Theory does not offer any direct insights either. Although there have been computational studies of the instabilities of three-dimensional flows, these models have not yet been extended to address the question of interest here.

For $\sigma = 19$, heat-transport measurements and some of the associated flow patterns are illustrated in figure 14. For this Prandtl number, a six-roll pattern is distorted by the cross-roll instability for all Rayleigh numbers. Although there are several pattern changes in the time-dependent regime for $R > 40R_c$, the mean Nusselt number seems to be influenced very little by the dominant pattern (imposed on a turbulent background). For $44R_c \lesssim R \lesssim 56R_c$, there is a strong oscillation of the flow boundaries with a period of several seconds. For $56R_c \lesssim R \lesssim 61R_c$, the dominant convective flow boundaries wander slowly, twist, break up and re-form; it appears that the natural wavelength of the flow is mismatched with the container dimensions for this range of Rayleigh numbers. For $R > 61R_c$, there appears to be spoke-pattern convection for which two adjacent spoke-pattern cells fill the container. Whitehead & Chan (1976) observed similar spoke patterns in a large container at lower Rayleigh numbers.

6. Summary

It is clear that changes in heat transport are closely related to changes in the flow pattern, and that these changes are significantly influenced by the container geometry. The studies of Davis (1967), Catton (1972 a, b), B. F. Edwards (1986, private communication) and others have shown the strong influence of lateral boundaries on the critical Rayleigh number R_c. We have demonstrated experimentally that heat transport is also substantially influenced by the lateral boundaries and that, provided the convection is basically two-dimensional, the influence of the lateral boundaries can be represented by a boundary-layer model. While the details of the specific model presented here should not be taken too seriously, the model represents a useful tool for estimating quantitatively the influence of lateral boundaries on the heat transport of two-dimensional convection.

With a heuristic two-dimensional model in hand, we have been able to examine quantitatively perturbations in the heat transport due to three-dimensional instabilities. Pattern distortion initiated by the skewed-varicose or knot instabilities leads to a pattern of fewer rolls and causes a decrease in the heat transport. In bimodal convection, however, the heat transport is enhanced by the appearance of the cross-rolls. Finally, the onset of time-dependent behaviour seems to have no intrinsic effect on the mean Nusselt number unless it is associated with significant pattern changes.

Our observations of flow patterns very near R_c confirm that the flow is three-dimensional, as suggested by the calculations of B. F. Edwards (1986, private communication) and Greenside & Coughran (1984). For very large R, it is also clear that three-dimensional models are required to describe the flow properties including heat transport. For intermediate Rayleigh numbers we have shown that a two-dimensional model provides a good representation of the transport properties, provided the flow pattern is known and the effects of finite aspect ratio are included. That is, a model which includes both the fluid variables and the container geometry – R, σ, k and the container aspect ratios – is both necessary and sufficient to determine the heat transport accurately.

For a container of infinite aspect ratio, the Galerkin calculations predict that dN/dR monotonically decreases above R_c. Our model for the effects of finite aspect ratio shows a maximum in dN/dR for $R > R_c$ (i.e. for $\epsilon \sim 0.1$, choosing parameters typical of our experiments). Although our experiments are in good agreement with dN/dR for $\epsilon \gtrsim 1$, our present apparatus does not have the sensitivity near R_c to test this prediction.

Kinks in the slope of the experimental measurements of Nusselt versus Rayleigh number reported by many observers (cf. Krishnamurti 1973) now appear to be associated with transitions in the flow pattern, at least in the range of Rayleigh numbers ($R \lesssim 80R_c$) studied in our experiments. Perhaps there are also structural changes in the turbulent flow which account for the kinks in Nusselt versus Rayleigh curves at much higher Rayleigh numbers as discussed in §1.

Appendix A. Convection rolls parallel to sidewalls

The equation for the amplitude envelope for convection rolls parallel to sidewalls is given in §4.2:

$$\xi_0^2 \left(\frac{\partial^2 A_1}{\partial x^2} \right) = -\epsilon A_1 + g|A_1|^2 A_1, \tag{A 1}$$

with boundary conditions $A_1 = 0$ at $x = 0$, L.

Guyon & Rudnick (1968) have shown that the general form of (A 1),

$$\frac{\partial^2 X}{\partial x^2} = -X + X^3,$$

has the solution

$$X = \left(\frac{2k^2}{1+k^2} \right)^{\frac{1}{2}} \text{sn} \left(\frac{x}{(1+k^2)^{\frac{1}{2}}} + \phi, \, k \right),$$

where sn is a Jacobi elliptic function of modulus k†, and ϕ and k are determined by boundary conditions.

Hence the solution to (A 1) can be written

$$A_1 = \left(\frac{\epsilon}{g} \right)^{\frac{1}{2}} \left(\frac{2k^2}{1+k^2} \right)^{\frac{1}{2}} \text{sn}(px + c, \, k), \tag{A 2}$$

where $p^2 = \epsilon/\xi_0^2(1+k^2)$. The boundary condition $A_1 = 0$ at $x = 0$ gives $c = 0$, and the condition $A_1 = 0$ at $x = L$ leads to

$$pL = 2nK(k), \tag{A 3}$$

where $K(k)$ is the complete elliptic integral of the first kind, and n is an integer. The only non-zero, dynamically stable solution is for $n = 1$ (Wesfried *et al.* 1978), so that (A 3) becomes

$$\frac{\epsilon^{\frac{1}{2}} L}{2\xi_0} = (1+k^2)^{\frac{1}{2}} K(k). \tag{A 4}$$

Since $K(k)$ is defined only for $0 \leqslant k \leqslant 1$, we find that a solution to (A 4) exists (i.e. that convection is possible) only for ϵ larger than $\epsilon_c = \pi^2 \xi_0^2/L^2$. For ϵ near ϵ_c (i.e. for $k \to 0$) the envelope amplitude approaches a sinusoidal shape

$$A_1 = \left(\frac{\epsilon}{g} \right)^{\frac{1}{2}} \frac{2}{(3\epsilon_c)^{\frac{1}{2}}} (\epsilon - \epsilon_c)^{\frac{1}{2}} \sin \left(\frac{\pi x}{L} \right),$$

while for large ϵ (i.e. $pL \gg 1$, $k \to 1$) the boundary layer near each wall takes the form (Wesfried *et al.* 1978)

$$A_1 = \left(\frac{\epsilon}{g} \right)^{\frac{1}{2}} \tanh (px), \quad x < \tfrac{1}{2}L.$$

The heat flux is computed from the definition in §4.2 with

$$|\psi|^2 = \frac{1}{L} \int_0^L A_1^2 \, dx. \tag{A 5}$$

---

† In this Appendix only, k is the modulus of the elliptic functions; elsewhere it represents roll wavenumber.
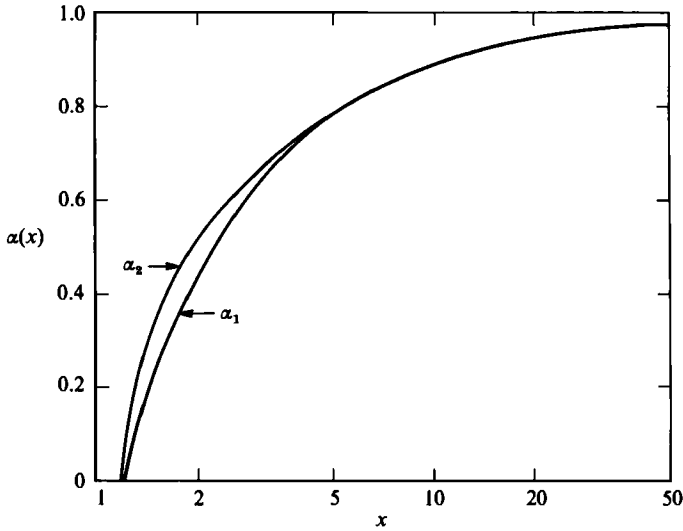
FIGURE 15. Heat-transport attenuation coefficients α_1 as a function of $\epsilon^{\frac{1}{2}}L$ and α_2 as a function of $\epsilon^{\frac{1}{2}}M$. (α_1 and α_2 are defined in Appendices A and B respectively.)

Using the substitution $u = px$,

$$|\psi|^2 = \left(\frac{1}{pL}\right)\frac{\epsilon}{g}\left(\frac{2k^2}{1+k^2}\right)\int_0^{pL} \mathrm{sn}^2\,(u,\,k)\,\mathrm{d}u$$

$$= \frac{1}{pL}\frac{\epsilon}{g}\left(\frac{2k^2}{1+k^2}\right)\left[\frac{1}{k^2}(pL - E(\mathrm{am}\,(pL),\,k))\right],$$

where E is the elliptic integral of the second kind and am is the elliptic amplitude. Using the boundary condition (A 4) and the identity $E(\mathrm{am}(K(k),\,k)) = E(k)$,

$$|\psi|^2 = \frac{\epsilon}{g}\left(\frac{2}{1+k^2}\right)\left[1 - \frac{E(k)}{K(k)}\right], \qquad\qquad (\mathrm{A}\ 6)$$

where k is determined from (A 3). In (A 6) g is a function of Prandtl number computed by Schluter *et al.* (1965) and Cross (1980) for the case of rigid horizontal boundaries, and ξ_0^2 is the curvature of the neutral stability curve at its minimum at $R = R_c$. For rigid boundaries, $\xi_0^2 = 0.148$.

The solution (A 6) may be written as the product

$$|\psi|^2 = f(\epsilon)\,\alpha_1(\epsilon,\,L),$$

where $f(\epsilon) = (\epsilon/g)$ is the asymptotic solution for $L \to \infty$, and

$$\alpha_1(\epsilon,\,L) = \left(\frac{2k^2}{1+k^2}\right)\left[1 - \frac{E(k)}{K(k)}\right]$$

represents the attenuation due to finite aspect ratio.

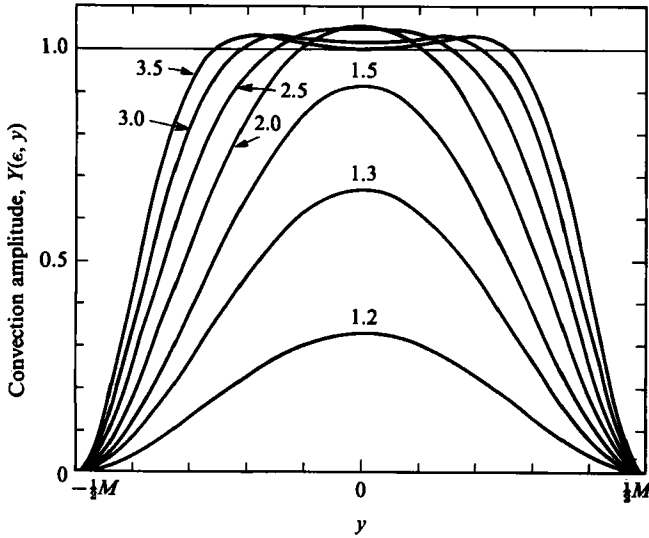Figure 15 illustrates α_1 as a function of ϵ and L.

FIGURE 16. Convective amplitude envelope for sidewalls perpendicular to the convective rolls (figure 8*b*) for various values of $\epsilon^{\frac{1}{4}}M$.

Appendix B. Convection rolls perpendicular to sidewalls

The equation for the amplitude envelope for rolls perpendicular to sidewalls at $y = \pm\frac{1}{2}M$ is given in §4.2:

$$\frac{\xi_0^2}{4q_0^2}\left(\frac{\partial^4 A_2}{\partial y^4}\right) = \epsilon A_2 - g|A_2|^2 A_2, \tag{B 1}$$

with boundary conditions $A_2 = \partial A_2/\partial y = 0$ at $y = \pm\frac{1}{2}M$.

The scaled form of this equation is

$$\frac{\partial^4 Y}{\partial y^4} = Y - Y^3, \tag{B 2}$$

for which a solution can be obtained by numerical methods in the form

$$Y(y) = \sum_{i=0}^{\infty} a_i y^i, \tag{B 3}$$

where the a_i depend on the boundary conditions. Then the solution to (B 1) may be written

$$A_2 = \left(\frac{\epsilon}{g}\right)^{\frac{1}{2}} Y\left(\epsilon^{\frac{1}{4}}\left(\frac{2q_0}{\xi_0}\right)^{\frac{1}{2}}y\right). \tag{B 4}$$

The critical wavenumber $q_0 = 3.117$; ξ_0 and g are defined in Appendix A.

Representative solutions to (B 1) are illustrated in figure 16. For the boundary conditions indicated above, there is a minimum ϵ for which a non-zero solution exists (i.e. for which convection is possible) given by

$$\epsilon_c = \left(\frac{\xi_0^2}{4q_0^2}\right)\left(\frac{4.730}{M}\right)^4.$$

For small ϵ, a Fourier expansion of amplitude envelope is dominated by the Fourier component $\cos^2(\pi x/M)$. For large ϵ the central region is nearly uniform in amplitude, while there are sharply defined boundary layers at each sidewall.

The heat flux is computed numerically from the definition in §4.2 with

$$|\psi|^2 = \frac{1}{M} \int_{-\frac{1}{2}M}^{\frac{1}{2}M} A_2^2 \, \mathrm{d}y. \tag{B 5}$$

Solutions to (B 5) can be written as the product

$$|\psi|^2 = f(\epsilon) \, \alpha_2(\epsilon, M)$$

where $f(\epsilon) = (\epsilon/g)$ is the asymptotic solution for $M \to \infty$, and $\alpha_2(\epsilon, M)$ represents the attenuation due to finite aspect ratio. The attenuation coefficient $\alpha_2(\epsilon, M)$ is illustrated in figure 15.

REFERENCES

AHLERS, G., CROSS, M. C., HOHENBERG, P. C. & SAFRAN, S. 1981 The amplitude equation near the convective threshold: application to time-dependent heating experiments. *J. Fluid Mech.* **110**, 297–334.

BEHRINGER, R. P. & AHLERS, G. 1982 Heat transport and temporal evolution of fluid flow near the Rayleigh–Bénard instability in cylindrical containers. *J. Fluid Mech.* **125**, 219–258.

BROWN, S. N. & STEWARTSON, K. 1977 On thermal convection in a large box. *Stud. Appl. Maths* **57**, 187–204.

BUSSE, F. H. 1967 On the stability of two-dimensional convection in a layer heated from below. *J. Math. Phys.* **46**, 140–150.

BUSSE, F. H. 1978 Non-linear properties of thermal convection. *Rep. Prog. Phys.* **41**, 1929–1967.

CATTON, I. 1970 Convection in a closed rectangular region: the onset of motion. *Trans. ASME* C: *J. Heat Transfer* **92**, 186–188.

CATTON, I. 1972a The effect of insulating vertical walls on the onset of motion in a fluid heated from below. *J. Heat Mass Transfer* **15**, 665–672.

CATTON, I. 1972b Effect of wall conduction on the stability of a fluid in a rectangular region heated from below. *Trans. ASME* C: *J. Heat Transfer* **94**, 446–452.

CHANDRASEKHAR, S. 1961 *Hydrodynamic and Hydromagnetic Stability*. Clarendon.

CHARLSON, G. S. & SANI, R. L. 1970 Thermoconvective instability in a bounded cylindrical fluid layer. *Intl J. Heat Mass Transfer* **13**, 1479–1496.

CHU, T. Y. & GOLDSTEIN, R. J. 1973 Turbulent convection in a horizontal layer of water. *J. Fluid Mech.* **60**, 141–159.

CLEVER, R. M. & BUSSE, F. H. 1974 Transition to time-dependent convection. *J. Fluid Mech.* **65**, 625–645.

CROSS, M. C. 1980 Derivation of the amplitude equation at the Rayleigh–Bénard instability. *Phys. Fluids* **23**, 1727–1731.

CROSS, M. C., DANIELS, P. G., HOHENBERG, P. C. & SIGGIA, E. D. 1980 Effect of distant sidewalls on wave-number selection in Rayleigh–Bénard convection. *Phys. Rev. Lett.* **45**, 898–901.

CROSS, M. C., DANIELS, P. G., HOHENBERG, P. C. & SIGGIA, E. D. 1983 Phase-winding solutions in a finite container above the convective threshold. *J. Fluid Mech.* **127**, 155–183.

DANIELS, P. G. 1977 The effect of distant sidewalls on the transition to finite amplitude Bénard convection. *Proc. R. Soc. Lond.* A **358**, 173–197.

DAVIES-JONES, R. P. 1970 Thermal convection in an infinite channel with no-slip sidewalls. *J. Fluid Mech.* **44**, 695–704.

DAVIS, S. H. 1967 Convection in a box: linear theory. *J. Fluid Mech.* **30**, 465–478.

DENNY, V. E. & CLEVER, R. M. 1974 Comparisons of Galerkin and finite difference methods for solving highly nonlinear thermally driven flows. *J. Comp. Phys.* 16, 271–284.

FRICK, H., BUSSE, F. H. & CLEVER, R. M. 1983 Steady three-dimensional convection at high Prandtl numbers. *J. Fluid Mech.* 127, 141–153.

GREENSIDE, H. S. & COUGHRAN, W. M. 1984 Nonlinear pattern formation near the onset of Rayleigh–Bénard convection. *Phys. Rev.* A30, 398–428.

GUYON, E. & RUDNICK, I. 1968 Size effects in superfluid helium II. I. Experiments in porous systems. *J. Phys. Paris* 29, 1081–1095.

KOLODNER, P., WALDEN, R. W., PASSNER, A. & SURKO, C. M. 1986 Rayleigh–Bénard convection in an intermediate-aspect-ratio rectangular container. *J. Fluid Mech.* 163, 195–226.

KRISHNAMURTI, R. 1970a On the transition to turbulent convection. Part 1. The transition from two- to three-dimensional flow. *J. Fluid Mech.* 42, 295–307.

KRISHNAMURTI, R. 1970b On the transition to turbulent convection. Part 2. The transition to time-dependent flow. *J. Fluid Mech.* 42, 309–320.

KRISHNAMURTI, R. 1973 Some further studies on the transition to turbulent convection. *J. Fluid Mech.* 60, 285–303.

LIPPS, F. B. & SOMERVILLE, R. C. J. 1971 Dynamics of variable wavelength in finite-amplitude Bénard convection. *Phys. Fluids* 14, 759–765.

LUIJKX, J. M. & PLATTEN, J. K. 1981 On the onset of free convection in a rectangular channel. *J. Non-Equilibr. Thermodyn.* 6, 141–158.

MALKUS, W. V. R. 1954a Discrete transitions in turbulent convection. *Proc. R. Soc. Lond.* A 225, 185–195.

MALKUS, W. V. R. 1954b The heat transport and spectrum of thermal turbulence. *Proc. R. Soc. Lond.* A 225, 196–212.

MOTSAY, R. W., ANDERSON, K. E. & BEHRINGER, R. P. 1988 The onset of convection and turbulence in rectangular layers of liquid helium. *J. Fluid Mech.* (in press).

NEWELL, A. C. & WHITEHEAD, J. A. 1969 Finite bandwidth, finite amplitude convection. *J. Fluid Mech.* 38, 279–303.

PLOWS, W. H. 1968 Some numerical results for two-dimensional steady laminar Bénard convection. *Phys. Fluids* 11, 1593–1599.

ROSSBY, H. T. 1969 A study of Bénard convection with and without rotation. *J. Fluid Mech.* 36, 309–335.

SCHLUTER, A., LORTZ, D. & BUSSE, F. H. 1965 On the stability of finite amplitude convection. *J. Fluid Mech.* 23, 129–144.

SEGEL, L. A. 1969 Distant side-walls cause slow amplitude modulation of cellular convection. *J. Fluid Mech.* 38, 203–224.

STORK, K. & MÜLLER, U. 1972 Convection in boxes: experiments. *J. Fluid Mech.* 54, 599–611.

THRELFALL, D. C. 1975 Free convection in low-temperature gaseous helium. *J. Fluid Mech.* 67, 17–28.

WALDEN, R. W., KOLODNER, P., PASSNER, A. & SURKO, C. M. 1984 Nonchaotic Rayleigh–Bénard convection with four and five incommensurate frequencies. *Phys. Rev. Lett.* 53, 242–245.

WESFREID, J., POMEAU, Y., DUBOIS, M., NORMAND, C. & BERGÉ, P. 1978 Critical effects in Rayleigh–Bénard convection. *J. Phys. Lett.* 39, 725–731.

WHITEHEAD, J. A. & CHAN, G. L. 1976 Stability of Rayleigh–Bénard convection rolls and bimodal flow at moderate Prandtl number. *Dyn. Atmos. Oceans* 1, 33–49.

WILLIS, G. E. & DEARDORFF, J. W. 1967 Confirmation and renumbering of the discrete heat flux transitions of Malkus. *Phys. Fluids* 10, 1861–1866.

WILLIS, G. E., DEARDORFF, J. W. & SOMERVILLE, R. C. J. 1972 Roll-diameter dependence in Rayleigh convection and its effect upon the heat flux. *J. Fluid Mech.* 54, 351–367.

ZALESKI, S., POMEAU, Y. & PUMIR, A. 1984 Optimal merging of rolls near a plane boundary. *Phys. Rev.* A 29, 366–370.